

Combined electron firehose and electromagnetic ion cyclotron instabilities: quasilinear approach

Z. Ali,¹ M. Sarfraz¹  and P. H. Yoon²

¹Department of Physics, GC University Lahore, Katchery Road, Lahore 54000, Pakistan

²Institute for Physical Science and Technology, University of Maryland, College Park, MD 20742, USA

Accepted 2020 September 18. Received 2020 September 15; in original form 2020 August 7

ABSTRACT

Various plasma waves and instabilities are abundantly present in the solar wind plasma, as evidenced by spacecraft observations. Among these, propagating modes and instabilities driven by temperature anisotropies are known to play a significant role in the solar wind dynamics. *In situ* measurements reveal that the threshold conditions for these instabilities adequately explain the solar wind conditions at large heliocentric distances. This paper pays attention to the combined effects of electron firehose instability driven by excessive parallel electron temperature anisotropy ($T_{\perp e} < T_{\parallel e}$) at high beta conditions, and electromagnetic ion cyclotron instability driven by excessive perpendicular proton temperature anisotropy ($T_{\perp i} > T_{\parallel i}$). By employing quasilinear kinetic theory based upon the assumption of bi-Maxwellian velocity distribution functions for protons and electrons, the dynamical evolution of the combined instabilities and their mutual interactions mediated by the particles is explored in depth. It is found that while in some cases, the two unstable modes are excited and saturated at distinct spatial and temporal scales, in other cases, the two unstable modes are intermingled such that a straightforward interpretation is not so easy. This shows that when the dynamics of protons and electrons are mutually coupled and when multiple unstable modes are excited in the system, the dynamical consequences can be quite complex.

Key words: instabilities – plasmas – methods: analytical – solar wind.

1 INTRODUCTION

Charged particles in the solar wind are detected to possess non-thermal features in their distributions, e.g. temperature anisotropies. Persistent observations made with space crafts such as *Helios*, *Ulysses*, and *Cluster* show the anisotropic behaviour of ions (Marsch et al. 1982; Marsch, Ao & Tu 2004; Marsch, Zhao & Tu 2006) and electrons (Štverák et al. 2008) for radial distances up to 5 au (astronomical unit). Under the dilute space plasma condition and in the absence of any significant heat flux, the kinetic instabilities play a key role in order to limit the unchecked increase in temperature anisotropies. Indeed, investigations report that the temperature anisotropies are partially bounded by marginal stability conditions of various plasma instabilities, which shows that simple fluid theory is not completely adequate for the description of solar wind dynamics (Chew, Goldberger & Low 1956). Note, however, that more sophisticated fluid approach may partially account for the observed temperature anisotropy boundaries (Hunana & Zank 2017). In general, kinetic theory, which incorporates wave–particle interactions, are more preferable for the complete description of quasi-isotropic state of solar wind particles subject to various instability criteria.

A useful practice adopted in the community is to plot the solar wind data in two-dimensional histogram in phase space formed by parameter $\beta_{\parallel a}$ and $T_{\perp a}/T_{\parallel a}$, for species $a = i, e$, where i and e stand for ions

(protons) and electrons, respectively. Here, $\beta_{\parallel a} = 8\pi n_0 T_{\parallel a}/B_0^2$ is the parallel plasma beta and $T_{\perp a}/T_{\parallel a}$ is temperature ratio for each species; $T_{\parallel a}$ and $T_{\perp a}$ represent parallel and perpendicular temperatures with respect to the ambient magnetic field, respectively; B_0 and n_0 are intensity of magnetic field and total density of particles, respectively. Such plots consistently demonstrate that the solar wind plasma is partially bounded by marginal stability conditions for various instabilities. For excessive perpendicular electron temperature anisotropy, $T_{\perp e} > T_{\parallel e}$, the observed data are bounded by marginal stability curve for electromagnetic electron-cyclotron instability. For the opposite case of $T_{\parallel e} > T_{\perp e}$, the same data coincide with parallel or oblique electron firehose instability threshold conditions. Similarly in case of ions, electromagnetic ion cyclotron (EMIC) or mirror instabilities are responsible for the bounded data under the higher ion perpendicular temperature condition $T_{\perp i} > T_{\parallel i}$, and marginal parallel or oblique proton firehose instability corresponds with bounded proton data at condition $T_{\parallel i} > T_{\perp i}$. Detailed descriptions of these micro-instabilities can be found in (Hasegawa 1975; Yoon 1992; Gary 1993; Yoon et al. 1993; Hellinger & Matsumoto 2000; Baumjohann & Treumann 2004; Hellinger et al. 2006, 2014; Yoon 2017).

The EMIC mode is left-handed (LH) circularly polarized mode, which is driven unstable by ion temperature anisotropy $T_{\perp i} > T_{\parallel i}$ and manifest maximum growth rate at $\mathbf{k} \times \mathbf{B}_0 = 0$ condition. While the observed solar wind data distribution at 1 au can be partially explained in terms of marginal EMIC instability condition, noticeable discrepancies also exist, especially for low beta regime for which, the mirror mode condition better explains the anisotropy upper bound. Significant attempts to improve the EMIC threshold condition have

* E-mail: sarfraz_gcu@yahoo.com

been made, which includes the introduction of different plasma compositions such as existence of alpha particles, including non-linear effects, improved modelling of proton distribution that modifies the shape of the distribution function as compared to simple bi-Maxwellian form, considering the presence of field aligned beams, and adopting non-thermal (supra-thermal) populations (Isenberg, Maruca & Kasper 2012; Maruca, Kasper & Gary 2012; Matteini et al. 2012). In pioneering works, Harris (1961) and Sagdeev & Shafranov (1961) studied the role of cyclotron instabilities in constraining the temperature anisotropies. Subsequently, such an idea was further extended to a wide variety of plasma environments (Schlickeiser & Skoda 2010; Maruca et al. 2012; Zhou et al. 2013; Chen et al. 2014; Gary et al. 2014; Omidi et al. 2014; Vinas et al. 2015). Furthermore, Shaaban et al. (2015, 2017) investigated the influence of electrons on the EMIC instability threshold condition on the basis of linear theory. These authors find that the interplay between anisotropic solar wind ions and electrons can significantly alter the EMIC marginal condition, a finding that is highly relevant to the present study.

In the literature, marginal EMIC instability condition is empirically modelled by a simple formula $T_{\perp i}/T_{\parallel i} = 1 + S\beta_{\parallel i}^{-\alpha}$, where (S , α) are empirically determined parameters. In order to determine these parameters, Gary et al. (1994) employed linear kinetic theory and suggested (0.42, 0.43). On the other hand, by employing the hybrid simulation analysis, the same authors determined (0.41, 0.44). On the basis of observations, Anderson et al. (1996) deduced the values (0.85, 0.48), while Phan et al. (1994) arrived at somewhat different values of (0.58, 0.53).

Electron firehose (EFH) mode is also a left-handed circularly polarized mode, which is driven unstable by higher electron parallel temperature than perpendicular temperature, $T_{\parallel e} > T_{\perp e}$, under high beta conditions. In the literature, the EFH instability has been extensively studied employing bi-Maxwellian model distributions, e.g. (Hollweg 1974), anisotropic supra-thermal distributions such as bi-kappa model, e.g. (Lazar & Poedts 2009a; Lazar et al. 2017), etc. A comparative study of EFH instability with Weibel (Lazar & Poedts 2009b) and ordinary mode (Lazar et al. 2014) instability is also a significant part of the literature. The electron firehose instability operative in oblique propagation direction has also been investigated in the literature (Paesold & Benz 1999; Li & Habbal 2000; Gary & Nishimura 2003; Camporeale & Burgess 2008; Hellinger et al. 2014). In this paper, we restrict ourselves to the parallel EFH instability, but unlike some previous works, we go beyond linear analysis and employ quasilinear method. We leave the similar quasilinear analysis of obliquely propagating firehose mode as a future research task. It should be mentioned that in all the aforementioned works on parallel or oblique firehose instability, the role of ions are minimized by assuming them to be thermally isotropic. Under such an assumption, the marginal stability condition for EFH instability depends only on $T_{\perp e}/T_{\parallel e}$ and $\beta_{\parallel e}$. As a result, the threshold condition can be empirically determined again by a simple formula, $T_{\perp e}/T_{\parallel e} = 1 - S\beta_{\parallel e}^{-\alpha}$, where S and α are the fitting parameters (Lazar et al. 2014).

In earlier studies, the influence of electrons on the dispersion characteristics of EMIC mode was ignored assuming them as non-resonant and thermally isotropic. In reality, the electrons under the condition, $T_{\parallel e} \neq T_{\perp e}$, can alter the stability characteristics of EMIC mode. Similarly, ions are assumed thermally isotropic in highlighting the wave-spectrum of EFH instability, most notable exception being the works by Shaaban et al. (2015) and Shaaban et al. (2017), as already mentioned. However, anisotropic ions may impact the stability characteristics of EFH mode, as shown by Shaaban et al. (2015, 2017). The dynamically coupled electrons and ions via mutual

influence on EMIC and EFH mode excitations may be important for the solar wind dynamics. In this regard, Yoon & Sarfraz (2017) and Yoon et al. (2019) investigated the importance of such a dynamical coupling between the electrons and protons in the global evolution of solar wind, and demonstrated that such a coupling may significantly contribute towards explaining the near isotropic conditions of the solar wind protons and electrons near 1 au. Since the analyses by Yoon & Sarfraz (2017) and Yoon et al. (2019) are global, for which the impacts of radial expansion, collisions as well as the instabilities are all incorporated, the individual properties of each process are obscured and difficult to separate.

In the present analysis, we revisit the issue of detailed dynamics associated with the combined EFH and EMIC instabilities. This is important since the two instabilities operate on different temporal and spatial scales. Global calculations such as those carried out by Yoon & Sarfraz (2017) and Yoon et al. (2019) generally assume a fixed spatial scale for the wave modes and fixed temporal time-steps in numerically advancing the global model equations. However, since the fast growing EFH mode involves short spatial scales while EMIC mode operates on long spatial scales, one may easily miss some important unstable wavenumber domain unless a care is exercised. Moreover, since EFH mode grows and saturates rapidly, the temporal discretization associated with any numerical global modelling effort may easily miss the most important small time scale phenomena associated with EFH instability. Note that Yoon & Sarfraz (2017) and Yoon et al. (2019) adopted a reduced model of the solar wind such that problems associated with multiscales are minimized. However, if one attempts to extend the scaled solar wind model to a realistic one, then one must exercise caution.

This has motivated us to re-examine the combined EFH/EMIC instability development by means of velocity moment-based quasilinear analysis under the assumption of bi-Maxwellian velocity distribution functions for the particles. The present study is further motivated by the proton and electron data taken with spacecraft near 1 au (Lin et al. 1995; Ogilvie et al. 1995; Maruca & Kasper 2013; Wilson et al. 2018), which show that anisotropic proton and temperatures with varying degree of parallel beta conditions characterize the solar wind near 1 au. See also, Hellinger et al. (2006) and Štverák et al. (2008). In particular, according to Wilson et al. (2018) a long duration (~ 10 yr) statistical analysis indicates that the electrons on average show higher temperature (thus, beta) than the protons, a condition favourable for combined EMIC and EFH instability excitation. Note also that the quasilinear scheme similar to our has already been successfully employed for a number of problems, including the proton-driven temperature anisotropy instabilities (Seough & Yoon 2012; Yoon & Seough 2012, 2014; Seough et al. 2013) and electron anisotropy-driven instabilities (Yoon et al. 2011; Sarfraz et al. 2016, 2017), and verified against particle-in-cell simulations. Such preliminary studies provide justifications for employing the velocity moment-based quasilinear methodology. Further, quasilinear method has been successfully employed for the single mode excitation cumulatively by two distinct populations of solar wind electrons e.g. thermal and suprathermal, considering their anisotropic temperatures (Lazar et al. 2018; Shaaban et al. 2019a) and combining with their relative drifts (Shaaban et al. 2019b; Shaaban & Lazar 2020). As noted, interplay of EMIC and EFH modes has been inherently considered within the reduced model of the global solar wind, without collisions (Yoon & Sarfraz 2017) and with collision effects (Yoon et al. 2019), but the details are obscured. This paper aims to re-examine this issue more carefully.

The structure of this paper is as follows: In Section 2, we will briefly discuss the linear and quasilinear theory of combined EMIC

and EFH instability. Section 3 will present the numerical solutions. A brief summary and discussion are given in Section 4.

2 MACROSCOPIC KINETIC MODEL OF THE SOLAR WIND BULK PARAMETERS

For a homogeneous plasma immersed in a uniform static magnetic field, we assume that the velocity distribution functions for electrons ($a = e$) and protons ($a = i$) are given by bi-Maxwellian forms, which are presumed to represent the plasma state for all time,

$$f_a = \frac{1}{\pi^{3/2} \alpha_{\perp a}^2(t) \alpha_{\parallel a}(t)} \exp \left(-\frac{v_{\perp}^2}{\alpha_{\perp a}^2(t)} - \frac{v_{\parallel}^2}{\alpha_{\parallel a}^2(t)} \right), \quad (1)$$

except that perpendicular and parallel temperatures may evolve in time t . In equation (1), $\alpha_{\perp a}$ and $\alpha_{\parallel a}$ stand for perpendicular and parallel thermal speeds of species labelled a , and are defined via

$$\begin{aligned} T_{\perp a} &= \frac{m_a}{2} \int dv v_{\perp}^2 f_a = \frac{m_a \alpha_{\perp a}^2}{2}, \\ T_{\parallel a} &= m_a \int dv v_{\parallel}^2 f_a = \frac{m_a \alpha_{\parallel a}^2}{2}. \end{aligned} \quad (2)$$

In the present definitions of temperature, the customary Boltzmann constant is omitted since we adopt eV for thermal energy unit. The analytical model distribution defined for proton-electron plasma is assumed for the solar wind conditions for which energetic events such as solar mass ejections are absent. We also assume that field-aligned streaming components, which are common for fast wind, are also absent. Specifically, we ignore any net relative drift between plasma components, which may be an additional free energy source for drift related instabilities, e.g. whistler heat flux instability and beam electron firehose instability (Gary 1993).

Note that our assumption of bi-Maxwellian model distribution is an approximation. Actual simulation results such as those by Gary, Vazquez & Winske (1996), Matteini et al. (2006), and Hellinger et al. (2014) depict the deviation of distribution from strict bi-Maxwellian form in the non-linear regime. Such a discrepancy notwithstanding, we maintain that the assumption of bi-Maxwellian model is a fairly reasonable representation as we are particularly interested in the temperature anisotropy-driven instabilities for which, during the instability development, the bulk of ions and electrons take part in resonant wave-particle interactions. Consequently, small deviations from strict bi-Maxwellian form do not seem to affect the dynamics in a fundamental manner. Indeed, a number of simulations performed previously (Seough, Yoon & Hwang 2014, 2015a; Seough et al. 2015b; Yoon et al. 2015, 2017) support our assumption regarding the particle distributions.

3 TRANSVERSE MODES: PARALLEL PROPAGATION

The present section details the mathematical background for dispersion characteristics of EMIC and EFH mode and adiabatic time evolution of initial distributions of protons and electrons in response to the instability development. We are particularly interested in the branch of ion cyclotron and electron firehose modes that are propagating strictly parallel (or antiparallel) to the static magnetic field. General non-relativistic dispersion relation can be found in standard literature, e.g. (Gary 1993; Schlickeiser 2002). For a homogeneous and dilute space plasmas (non-collisional) the dispersion relation of

interest reads as follows:

$$\begin{aligned} \frac{c^2 k^2}{\omega^2} &= 1 + \sum_{a=i,e} \frac{\omega_{pa}^2}{\omega^2} \int dv \frac{v_{\perp}/2}{\omega - kv_{\parallel} \pm \Omega_a} \\ &\times \left((\omega - kv_{\parallel}) \frac{\partial f_a}{\partial v_{\perp}} + kv_{\perp} \frac{\partial f_a}{\partial v_{\parallel}} \right), \end{aligned} \quad (3)$$

where ω and k are, respectively, the angular frequency and wavenumber of the mode; v_{\perp} and v_{\parallel} are representations of velocity components perpendicular and parallel to the external magnetic field, respectively; $\omega_{pa} = (4\pi n_0 e^2/m_a)^{1/2}$ is the plasma frequency and $\Omega_a = eB_0/m_a c$ represents the cyclotron frequency of species of sort a ; m_a is the mass of species of labelled as a ; e is unit electric charge; c represents the speed of light in *vacuo*; n_0 stands for the total number density; B_0 denotes the intensity of ambient magnetic field; \pm designate the right-handed (RH) versus left-handed (LH) circularly polarized electromagnetic modes, for upper and lower signs, respectively. Many authors have utilized dispersion relation (3) to analyse the parallel-propagating instabilities driven by excessive parallel ($T_{\parallel} > T_{\perp}$) or perpendicular ($T_{\perp} > T_{\parallel}$) temperature anisotropy (Dum, Marsch & Pilipp 1980; Wu, Yoon & Freund 1989; Lazar & Poedts 2009b; Schlickeiser, Lazar & Skoda 2011; Vinas et al. 2014; Lazar et al. 2015; Shaaban et al. 2016).

Making an allowance for adiabatic bi-Maxwellian distribution function (1) for ions (protons) and electrons, the following instantaneous dispersion relation for left-hand circularly polarized transverse electromagnetic mode emerges:

$$\begin{aligned} 0 &= \frac{c^2 k^2}{\omega_{pi}^2} - A_i - \frac{(A_i + 1)\omega - A_i \Omega_i}{k \alpha_{\parallel i}} Z \left(\frac{\omega - \Omega_i}{k \alpha_{\parallel i}} \right) \\ &\quad - \frac{m_i}{m_e} \left[A_e + \frac{(A_e + 1)\omega + A_e \Omega_e}{k \alpha_{\parallel e}} Z \left(\frac{\omega + \Omega_e}{k \alpha_{\parallel e}} \right) \right], \\ A_i &= \frac{T_{\perp i}}{T_{\parallel i}} - 1, \quad A_e = \frac{T_{\perp e}}{T_{\parallel e}} - 1, \end{aligned} \quad (4)$$

where the plasma dispersion function (Fried 1961) is defined by, $Z(\zeta) = \int_{-\infty}^{\infty} (x - \zeta)^{-1} e^{-x^2} dx$, for $\text{Im}(\zeta) > 0$. For $\text{Im}(\zeta) < 0$ it is understood that analytic continuation is to be employed. In (4), we have ignored the displacement current as we are not interested in fast transverse modes. The dispersion relation applies adiabatically to all time as the temporal variations enter through the temperatures of ions and electrons.

The modifications in initial distributions are studied with the aid of particle kinetic equation. Under the diffusion approximation and strictly parallel propagation condition, the form of particle kinetic equation subject to excitation of EMIC and EFH modes is

$$\begin{aligned} \frac{\partial f_a}{\partial t} &= \frac{ie^2}{4m_a^2 c^2} \frac{1}{v_{\perp}} \int_{-\infty}^{\infty} \frac{dk}{k^2} \mathcal{L}^* \frac{v_{\perp} \delta B^2(k)}{\omega - kv_{\parallel} - \Omega_a} \mathcal{L} f_a, \\ \mathcal{L} &= (\omega - kv_{\parallel}) \frac{\partial}{\partial v_{\perp}} + kv_{\perp} \frac{\partial}{\partial v_{\parallel}}, \end{aligned} \quad (5)$$

where the asterisk denotes the complex conjugate, $\omega = \omega_k + i\gamma_k$ is the complex root of equation (3) – or (4) for that matter, and $\delta B^2(k)$ is the spectral wave energy density associated with magnetic field perturbations. The rigorous quasilinear theory comprises of directly solving the particle kinetic equation (5). In what follows, to reduce theory into *macroscopic* quasilinear approach, we take the velocity moments of (5). Specifically, velocity moments of interest are those that define perpendicular and parallel temperatures a la (2). Making

use of (5), and for bi-Maxwellian f_a , i.e. (1), we arrive at

$$\begin{aligned} \frac{dT_{\perp a}}{dt} &= -\frac{e^2}{2m_a c^2} \int \frac{dk}{k^2} \delta B^2(k) \left\{ (2A_a + 1) \gamma_k \right. \\ &\quad + \text{Im} \frac{2i\gamma - (\pm)^\sigma \Omega_a}{k\alpha_{\parallel a}} \\ &\quad \left. \times [(A_a + 1)\omega - (\pm)^\sigma A_a \Omega_a] Z(\zeta_a) \right\}, \\ \frac{dT_{\parallel a}}{dt} &= \frac{e^2}{m_a c^2} \int \frac{dk}{k^2} \delta B^2(k) \left\{ (A_a + 1) \gamma_k \right. \\ &\quad + \text{Im} \frac{\omega - (\pm)^\sigma \Omega_a}{k\alpha_{\parallel a}} \\ &\quad \left. \times [(A_a + 1)\omega - (\pm)^\sigma A_a \Omega_a] Z(\zeta_a) \right\}, \\ A_a &= \frac{T_{\perp a}}{T_{\parallel a}} - 1, \quad \zeta_a = \frac{\omega - (\pm)^\sigma \Omega_a}{k\alpha_{\parallel a}}, \end{aligned} \quad (6)$$

where $\sigma = +1$ corresponds to ions and $\sigma = -1$ is for electrons. The wave kinetic equation is given by the standard quasilinear form, namely, $\partial \delta B^2(k)/\partial t = 2\gamma_k \delta B^2(k)$.

4 NUMERICAL ANALYSIS

Numerical analysis starts with the introduction of following dimensionless (or normalized) quantities:

$$\begin{aligned} z &= \frac{\omega}{\Omega_i}, \quad q = \frac{ck}{\omega_{pi}} = \frac{kv_A}{\Omega_i}, \quad \tau = \Omega_i t, \quad M = \frac{m_i}{m_e}, \\ \beta_{\perp i} &= \frac{8\pi n_0 T_{\perp i}}{B_0^2} = \frac{\alpha_{\perp i}^2}{v_A^2}, \quad \beta_{\parallel i} = \frac{8\pi n_0 T_{\parallel i}}{B_0^2} = \frac{\alpha_{\parallel i}^2}{v_A^2}, \\ \beta_{\perp e} &= \frac{8\pi n_0 T_{\perp e}}{B_0^2} = \frac{\alpha_{\perp e}^2}{v_A^2} \frac{1}{M}, \quad \beta_{\parallel e} = \frac{8\pi n_0 T_{\parallel e}}{B_0^2} = \frac{\alpha_{\parallel e}^2}{v_A^2} \frac{1}{M}, \\ A_i &= \frac{T_{\perp i}}{T_{\parallel i}} - 1 = \frac{\beta_{\perp i}}{\beta_{\parallel i}} - 1, \\ A_e &= \frac{T_{\perp e}}{T_{\parallel e}} - 1 = \frac{\beta_{\perp e}}{\beta_{\parallel e}} - 1, \\ \zeta_i &= \frac{z - 1}{q\beta_{\parallel i}^{1/2}}, \quad \zeta_e = \frac{z + M}{q(M\beta_{\parallel e})^{1/2}}, \\ \eta_i &= \frac{(A_i + 1)z - A_i}{q\beta_{\parallel i}^{1/2}}, \quad \eta_e = \frac{M^{1/2}[(A_e + 1)z + MA_e]}{q\beta_{\parallel e}^{1/2}}, \\ W(q) &= \frac{\delta B^2(q)}{B_0^2}. \end{aligned} \quad (7)$$

The normalized equations that form the basis of numerical analysis are then given by

$$\begin{aligned} 0 &= q^2 - A_i - MA_e - \eta_i Z(\zeta_i) - \eta_e Z(\zeta_e), \\ \frac{d\beta_{\perp e}}{dt} &= - \int \frac{dq}{q^2} W(q) \{M(2A_e + 1)z_i \\ &\quad + \text{Im}(2iz_i + M)\eta_e Z(\zeta_e)\}, \\ \frac{d\beta_{\parallel e}}{dt} &= 2 \int \frac{dq}{q^2} W(q) \{M(A_e + 1)z_i \\ &\quad + \text{Im}(z + M)\eta_e Z(\zeta_e)\}, \\ \frac{d\beta_{\perp i}}{dt} &= - \int \frac{dq}{q^2} W(q) \{(2A_i + 1)z_i \\ &\quad + \text{Im}(2iz_i - 1)\eta_i Z(\zeta_i)\}, \end{aligned}$$

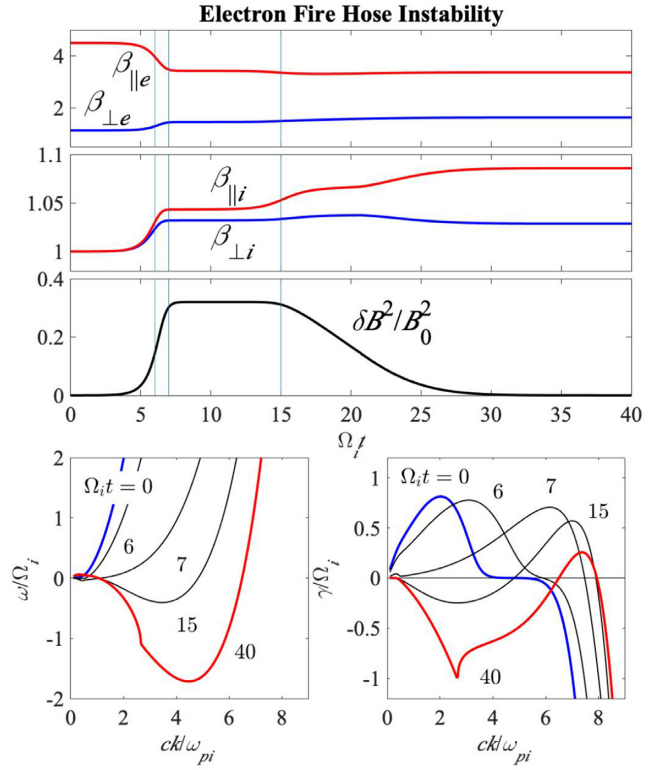


Figure 1. Sample results for EFH instability: Upper three panels display the time variation of electron betas, $\beta_{\perp e}$ and $\beta_{\parallel e}$, proton betas, $\beta_{\perp i}$ and $\beta_{\parallel i}$, and wave magnetic field energy density $\delta B^2/B_0^2$, versus normalized time $\Omega_i t$. Bottom dual panels plot the adiabatic variation in frequency, ω/Ω_i , and growth rate, γ/Ω_i , versus normalized wavenumber in various intermediate time-steps (indicated in the first three panels by vertical lines).

$$\begin{aligned} \frac{d\beta_{\parallel i}}{dt} &= 2 \int \frac{dq}{q^2} W(q) \{(A_i + 1)z_i \\ &\quad + \text{Im}(z - 1)\eta_i Z(\zeta_i)\}, \\ \frac{\partial W(q)}{\partial \tau} &= 2z_i W(q). \end{aligned} \quad (8)$$

4.1 Electron firehose instability: solar wind electrons with $T_{\perp e} < T_{\parallel e}$

Fig. 1 plots the numerical result of a sample case in which the EFH instability is initially excited by an excessive parallel electron temperature anisotropy ($T_{\perp e} < T_{\parallel e}$), while the protons are initially isotropic ($T_{\perp i} = T_{\parallel i}$). The initial conditions are specified by

$$\begin{aligned} \beta_{\perp e}(0)/\beta_{\parallel e}(0) &= 0.25, & \beta_{\parallel e}(0) &= 4.5, \\ \beta_{\perp i}(0)/\beta_{\parallel i}(0) &= 1, & \beta_{\parallel i}(0) &= 1. \end{aligned} \quad (9)$$

In all the numerical analyses discussed in this paper, we take the initial wave intensity level as $W(k, 0) = \delta B^2(k, 0)/B_0^2 = 10^{-5}$. The time evolution of beta's (dimensionless temperatures) is depicted in the top two panels. The top panel shows that the initial parallel electron temperature, or parallel beta $\beta_{\parallel e}$, is reduced as time progresses, while the perpendicular electron beta $\beta_{\perp e}$ increases in response to the excitation and subsequent saturation of the EFH instability. The second panel from top shows changes in the initially isotropic proton betas, $\beta_{\perp i}$ and $\beta_{\parallel i}$. The changes in these quantities are rather minimal (note the vertical scale). It is shown that the protons undergo weak

heating in both perpendicular and parallel directions, but slightly more along the parallel direction. The overall changes are less than 10 percent of their initial values. The third panel from top shows the net wave magnetic field energy density, $\delta B^2/B_0^2 = \int dq W(q)$, corresponding to EFH mode. It is seen that the wave energy first undergoes exponential rise followed by saturation. Subsequently, the wave energy is reabsorbed by the particles, presumably by the protons, as the protons resonantly interact with the left-hand mode, but also judging from the proton heating, such that the total wave energy density falls back down to the level of initial noise.

In the bottom dual panels, we plot the instantaneous dispersion relations, including the initial dispersion relation, shown with blue curves. The left- and right-hand panels depict the normalized real frequency z_r and normalized growth/damping rate z_i versus dimensionless wavenumber $q = ck/\omega_{pi}$, respectively. The instantaneous (or adiabatic) dispersion relations at three different intermediate time-steps after the initial time, namely, $\tau = \Omega_i t = 6, 7, 14$, are plotted with thin black curves. The dispersion relation corresponding to the final state, that is, at the end of the computation, $\tau = 40$, is depicted with red curves. In the top three panels, we have indicated with vertical lines the intermediate time-steps for which these adiabatic dispersion curves are plotted. As the adiabatic dispersion relation shows, the dispersion properties do not change much from the initial state $\tau = 0$ until $\tau = 6$ or so. From $\tau = 6$ to 7, the change is sudden and quite drastic. Further changes can be seen until $\tau = 15$, at which point, the wave energy density begins to be reabsorbed by the particles.

Note that in Fig. 1, the protons are heated in both directions but slightly higher along parallel direction. This is somewhat different from other known results, e.g. Messmer (2002), who show that oblique electron firehose instability leads to perpendicular proton heating. Our quasilinear calculation is restricted to parallel propagation so that a direct comparison with Messmer (2002) is not feasible, but related works (Sarfraz et al. 2017; Yoon et al. 2017) carried out quasilinear analysis of parallel electron firehose instability, which also show perpendicular proton heating. However, the parameter range adopted in (Sarfraz et al. 2017; Yoon et al. 2017) is different from the present input (9). In order to understand this behaviour, we have run two other cases besides the reference case, which is Fig. 1. That is, we have fixed all other input parameters as in (9), except that we have considered low initial parallel proton beta, $\beta_{ii}(0) = 0.5$ and another case with higher initial proton parallel beta, $\beta_{ii}(0) = 4$. That is, for the low proton beta case, we chose $\beta_{\perp e}(0)/\beta_{ie}(0) = 0.25$, $\beta_{ie}(0) = 4.5$, $\beta_{\perp i}(0)/\beta_{ii}(0) = 1$, and $\beta_{ii}(0) = 0.5$. The reference case, of course, is specified by (9). The high electron beta case refers to the input parameters $\beta_{\perp e}(0)/\beta_{ie}(0) = 0.25$, $\beta_{ie}(0) = 4.5$, $\beta_{\perp i}(0)/\beta_{ii}(0) = 1$, and $\beta_{ii}(0) = 4$. Fig. 2 shows that perpendicular proton heating takes place for the low proton beta case (left-most columns), but the standard case, which is already shown in Fig. 1 and the high electron beta case correspond to predominant parallel proton heating. This shows that the consequence of EFH instability excitation on the protons is far from being unilateral.

We have also plotted instantaneous dispersion relations for the three cases, that is, lower initial proton beta [$\beta_{ii}(0) = 0.5$], the standard case [$\beta_{ii}(0) = 1$], and higher initial proton parallel beta [$\beta_{ii}(0) = 4$], at normalized times $\Omega_i t = 0, 7, 15$, and 40. The result is displayed in Fig. 3. The results are reminiscent of the bottom double panels in Fig. 1. Of course, the standard case [middle columns] is identical to that of Fig. 1 bottom dual panels. We have shown the instantaneous dispersion relations for the other two cases,

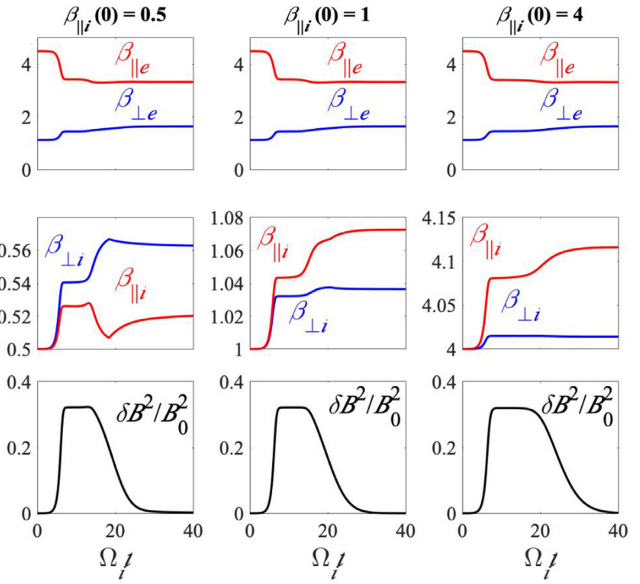


Figure 2. Quasilinear development of EFH instability with lower initial proton beta [$\beta_{ii}(0) = 0.5$], shown on the left three columns: The standard case [$\beta_{ii}(0) = 1$], shown in the middle three columns: and higher initial proton parallel beta [$\beta_{ii}(0) = 4$], shown on the right three columns. Perpendicular proton heating is observed for the low proton beta case (left-most panels), but for the reference case (middle columns) as well as for the high beta case (right-most case), parallel proton heating is dominant.

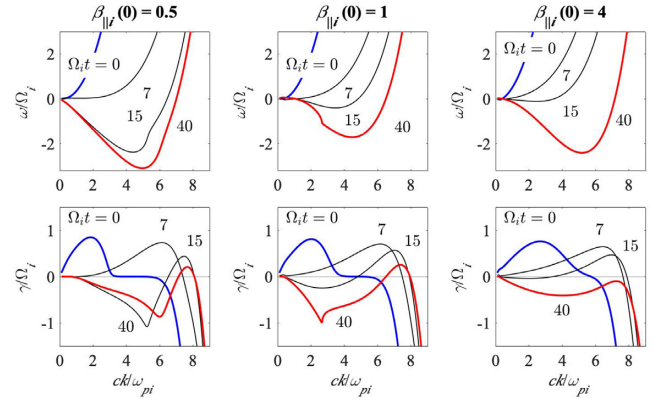


Figure 3. Instantaneous dispersion relations for unstable EFH mode for (left) lower initial proton beta [$\beta_{ii}(0) = 0.5$]; (middle) the standard case [$\beta_{ii}(0) = 1$]; and (right) and higher initial proton parallel beta [$\beta_{ii}(0) = 4$].

namely, low and high initial proton parallel beta cases, for the sake of completeness.

The purpose of Figs 1–3 is to highlight the salient features related to the unstable EFH mode and its dynamical properties, further details of which can be found in Sarfraz et al. (2017) and Yoon et al. (2017). These features are that EFH instability is excited rather quickly and saturated early. After saturation the wave energy density is reabsorbed by the particles, presumably by the protons. The dispersion relation for EFH instability features real frequency that shows broad frequency range that exceeds the proton cyclotron frequency and above. This case will be used in identifying the characteristics associated with EFH instability, which is to be distinguished from EMIC instability.

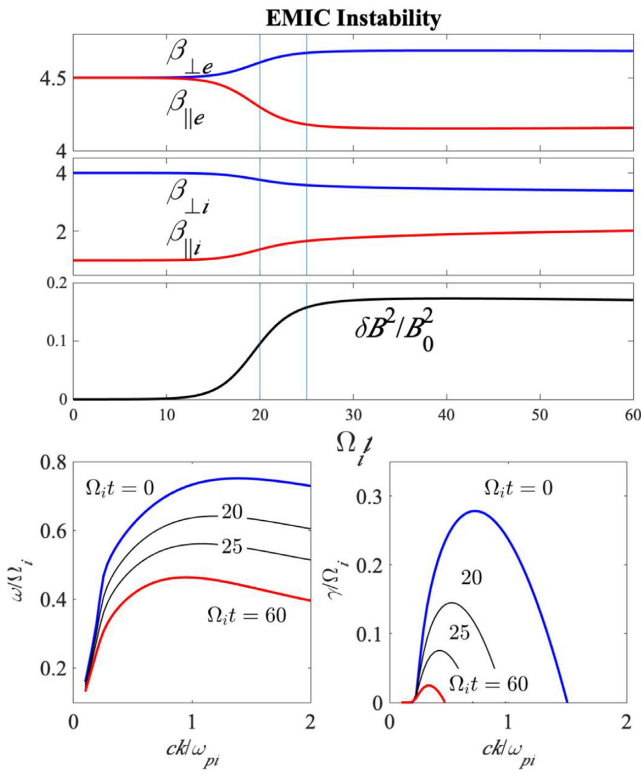


Figure 4. Sample results for EMIC instability: The format is the same as that of Fig. 1.

4.2 Electromagnetic ion cyclotron instability: solar wind ions with $T_{\perp i} > T_{\parallel i}$

Fig. 4 displays a sample case representing EMIC instability driven by an excessive perpendicular proton temperature anisotropy ($T_{\perp i} > T_{\parallel i}$). The electrons are initially assumed to be isotropic ($T_{\perp e} = T_{\parallel e}$). Quasilinear development of EMIC is well known, see e.g. Davidson & Ogden (1975), Seough & Yoon (2012) and Yoon & Seough (2012), but we replicate the known result here for the sake of later reference when both EFH and EMIC instabilities are excited simultaneously. Specifically, for Fig. 4, we adopt the following initial parameters:

$$\begin{aligned} \beta_{\perp e}(0)/\beta_{\parallel e}(0) &= 1, & \beta_{\parallel e}(0) &= 4.5, \\ \beta_{\perp i}(0)/\beta_{\parallel i}(0) &= 4, & \beta_{\parallel i}(0) &= 1. \end{aligned} \quad (10)$$

The top panel shows that the electrons undergo a mild perpendicular heating and parallel cooling, with the heating/cooling rates that are approximately 20 per cent of the initial temperatures. Note that in the customary quasilinear treatment of EMIC instability the electron dynamics is often ignored (Davidson & Ogden 1975; Seough & Yoon 2012; Yoon & Seough 2012). The second panel from top shows the expected result of gradual decrease in the initial proton temperature anisotropy by way of reduction of $\beta_{\perp i}$ and increase of $\beta_{\parallel i}$. The wave magnetic field energy density associated with EMIC instability shows an initial exponential increase followed by an eventual saturation in the time interval between $\Omega_i t = 20$ and $\Omega_i t = 30$. Note that the reabsorption of wave energy by the particle in the late stage after the saturation does not take place for EMIC instability (or at least it is not apparent). The bottom left- and right- panels plot the instantaneous dispersion relation at five different time-steps, at initial time $t = 0$, two intermediate times, $\Omega_i t = 20, 25$, and at final time $\Omega_i t = 60$. The initial dispersion relation is plotted with

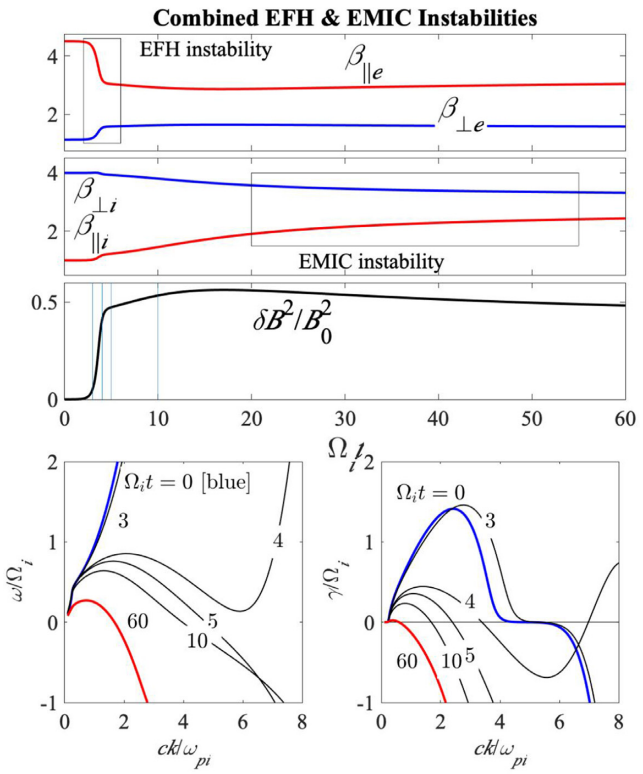


Figure 5. Sample results for combined EFH and EMIC instabilities: The format is the same as that of Fig. 1.

blue colour, while the final result is plotted by making use of red curves. The intermediate times are marked with vertical lines in the upper three panels. The distinguishing feature associated with EMIC instability is that the time scale is significantly longer than that of EFH instability so that when the two instabilities are initially operative one should be able to delineate one mode versus another. Another notable feature is that the real frequency associated with the instantaneous EMIC mode dispersion relation never exceeds the proton cyclotron frequency. The fact that the saturate wave energy density does not show any apparent reabsorption behaviour is already noted. Together with Fig. 1, the present quasilinear analysis of EMIC instability will be useful in interpreting the combined EFH and EMIC instabilities.

4.3 Combined EFH and EMIC instability: solar wind electrons with $T_{\perp e} < T_{\parallel e}$ and ions with $T_{\perp i} > T_{\parallel i}$

We present in Fig. 5 the quasilinear analysis of combined EFH (electron firehose) and EMIC (electromagnetic ion cyclotron) instabilities. We take the following initial parameters:

$$\begin{aligned} \beta_{\perp e}(0)/\beta_{\parallel e}(0) &= 0.25, & \beta_{\parallel e}(0) &= 4.5, \\ \beta_{\perp i}(0)/\beta_{\parallel i}(0) &= 4, & \beta_{\parallel i}(0) &= 1. \end{aligned} \quad (11)$$

In this case, both electrons and protons carry free energy sources as their initial temperatures are unequal. For electrons, the excessive parallel temperature anisotropy ($T_{\perp e} < T_{\parallel e}$) should drive EFH instability, while for protons, the excessive perpendicular temperature anisotropy ($T_{\perp i} > T_{\parallel i}$) should drive EMIC instability. These instabilities should proceed at different rates so that in principle one should be able to identify the developments of these two separate modes at different times. However, the matter is not as straightforward as

the dynamical properties of electrons and protons will be subject to influences from both unstable modes. Consequently, clear and unmistakable delineation of the two unstable mode may not always be so easy. The case shown in Fig. 4, however, falls into a category where the delineation is possible.

As indicated in the top two panels by rectangular boxes, the two distinct phases of EFH and EMIC instability developments can be identifiable. In specific, the top panel shows the rapid reduction of $\beta_{\parallel e}$ and a mild increase of $\beta_{\perp e}$, followed by saturation, which is similar to that shown in the top panel of Fig. 1. From the behaviour of electron temperature evolution and the associated time-scale, we thus conclude that the relatively early phase of the dynamics is dictated by EFH instability. In the second panel from top, the protons are seen to respond to the excitation of EFH instability during the relatively early phase, but only just so slightly, as not much appreciable changes can be detected in $\beta_{\perp i}$ and $\beta_{\parallel i}$ during the time range over which the electrons beta's undergo sudden changes. However, once the EMIC instability proper kicks in at a later time, the reduction of $\beta_{\perp i}$ and an increase in $\beta_{\parallel i}$, which are characteristic of EMIC quasilinear behaviour, are clearly seen. The dynamical phase of EMIC instability is indicated by the rectangular box. The electrons undergo some small yet noticeable dynamical changes during the EMIC instability phase. Specifically, it can be seen that $\beta_{\parallel e}$ undergoes a slight increase, albeit, the change is not so easy to detect visually. The wave energy density evolves in a manner consistent with EFH instability early on, but instead of the wave energy density being reabsorbed by the particles, the subsequent excitation of EMIC instability maintains the finite level of wave magnetic field energy density. The bottom two panels depict the snapshot of instantaneous dispersion relation. The time intervals are indicated by vertical lines in the third panel from top. These are initial time $t = 0$, intermediate times, $\Omega_i t = 3, 5, 10, 60$, and final time $\Omega_i t = 60$. From $t = 0$ and 3, the wave dispersion relation is dominated by EFH mode properties, but the dispersive characteristics gradually changes until the system is largely characterized by EMIC mode property by the time the system evolved to $\Omega_i t = 5$ and 10, or so. Specifically, going from $\Omega_i t = 3$ to 4, it can be seen that the real frequency changes from the EFH mode to that of EMIC mode in that the real frequency for the unstable range of wave numbers drops below the proton cyclotron frequency.

For this case, we thus conclude that a combined EFH and EMIC instabilities affect the properties of electrons and protons in different time-scales, and that the temporal profile of the wave energy density rather convincingly demonstrates the time evolution of two separate modes operating at distinct time scales. As it will be discussed subsequently, however, such a clear distinction is not always evident when the input parameters are changed. As one will see, quasilinear development of the combined EFH and EMIC instabilities can become quite complex such that linear theory alone cannot predict the outcome. Before we discuss such a complex case, however, let us discuss another case in which a clear distinction can arguably be made.

We thus consider the initial input parameters specified by

$$\begin{aligned} \beta_{\perp e}(0)/\beta_{\parallel e}(0) &= 0.25, & \beta_{\parallel e}(0) &= 4.5, \\ \beta_{\perp i}(0)/\beta_{\parallel i}(0) &= 4, & \beta_{\parallel i}(0) &= 10. \end{aligned} \quad (12)$$

In this case, other parameters are the same as those of Fig. 4 but the initial proton parallel beta is 10 times higher. In this case, obviously proton thermal energy is much higher so that EMIC instability will lead to a higher level of wave spectrum and also, EMIC instability proceeds faster. This makes the distinction between EFH and EMIC a bit difficult as the time scales between the two modes are not too

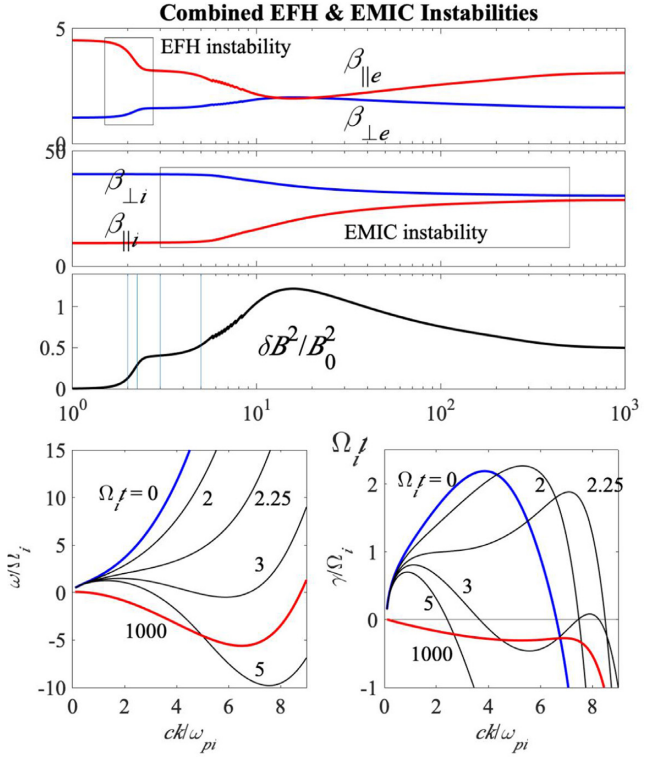


Figure 6. The same as Fig. 5, except that the proton beta's are initially 10 times higher.

different and as such, there is a certain overlap between the two modes as they progress in time. Indeed, numerical results reflect this expectation. This is shown in Fig. 6, where we plot the solutions in the same format as before. In the top panel early excitation of EFH mode and saturation leads to a reduction of parallel electron beta and a mild increase of perpendicular electron beta, thereby reducing the excessive parallel electron thermal anisotropy. As the second panel shows, protons do not undergo much changes during the early-time range. The third panel shows a trademark signature of early excitation and saturation of EFH mode. The instantaneous dispersion relations for $\Omega_i t = 0$ (initial state), 2, 2.25, bear clear signature of EFH mode. Between $\Omega_i t = 2.25$ and 3, however, the real frequency structure undergoes a significant change as the system takes on the characteristics of EMIC mode. From this point on, the system is governed by EMIC instability.

The characteristic EMIC development is reflected in the dynamical profiles of $\beta_{\perp i}$ and $\beta_{\parallel i}$, which are indicated by the rectangular box. An interesting feature associated with Fig. 6 is that the electrons respond to the later excitation of EMIC mode in a much more drastic way when compared to the previous case in which the proton parallel beta was initially given by $\beta_{\parallel i}(0) = 1$. In the present case with $\beta_{\parallel i}(0) = 10$, the electrons respond more appreciably, as can be seen in the top panel. The third panel shows that the wave magnetic field energy density increases in accordance with the dynamical changes in the particles. In this case, however, it can be seen that the EMIC wave energy is partially reabsorbed by the particles in late times, which is, of course, somewhat different than that of Fig. 5. In the present case of Fig. 6, because of the vastly different time-scales associated with EFH and EMIC instabilities, we adopted a logarithmic time axis.

The next case presented in Fig. 7 highlights the complexity associated with the combined instabilities and difficulties involved in their interpretation. For this case, we consider the input parameters

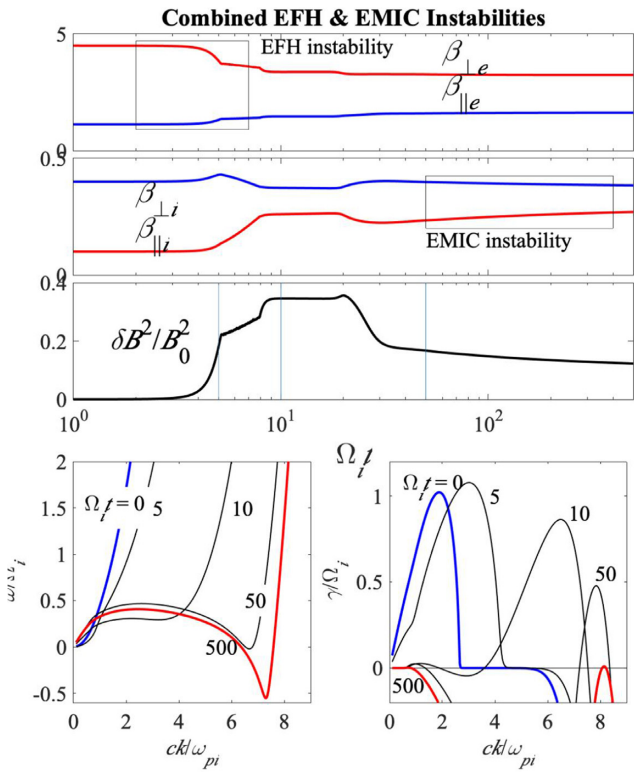


Figure 7. The same as Fig. 5 or Fig. 6, except that the initial proton beta's are 10 times lower than that of Fig. 5 and two orders of magnitude lower than that considered in Fig. 6.

specified by

$$\begin{aligned} \beta_{\perp e}(0)/\beta_{\parallel e}(0) &= 0.25, & \beta_{\parallel e}(0) &= 4.5, \\ \beta_{\perp i}(0)/\beta_{\parallel i}(0) &= 4, & \beta_{\parallel i}(0) &= 0.1. \end{aligned} \quad (13)$$

As is apparent, this choice of parameters is the same as in Fig. 5 (and also that of Fig. 6) except that we consider $\beta_{\parallel i}(0) = 0.1$. Recall that in Fig. 5, the same was chosen as $\beta_{\parallel i}(0) = 1$, while for Fig. 6, we considered $\beta_{\parallel i}(0) = 10$. Thus, the present case represents protons beta's ten times lower than that of Fig. 5 and a hundredfold lower than that of Fig. 6. In this case we again choose to plot the result making use of logarithmic time axis. Top panels show the typical dynamical profile for electron betas associated with EFH instability. This is no surprise. However, the second panel, which plots proton beta's, exhibit unexpectedly complex dynamical profile. During the time-scale associated with EFH excitation and saturation the protons undergo heating in both directions, which is somewhat expected. However, the subsequent evolution does not show any easily identifiable characteristics associated with the EMIC instability development. In fact, the proton beta's undergo a slight cooling, followed by saturation behaviour, then a slight reheating. Subsequently, the gradual decrease for $\beta_{\perp i}$ and increase in $\beta_{\parallel i}$ appear to represent a typical behaviour related to EMIC instability. For this reason, we have placed a rectangular box in the late-time domain, but this only represents an eyeball estimation rather than a rigorous identification.

The complex nature of the present case is even more highlighted by the behaviour associated with time evolution of wave energy density. The third panel from top shows that for early time, the system is indeed governed by the expected linear exponential growth phase of EFH instability, but instead of transitioning to a gradual and smooth

saturated wave intensity, there is kink in the slope of the time profile for $\delta B^2/B_0^2$. This kink is reflected in the dynamical profiles of the particle beta's as well. The time at which this happens is roughly $\Omega_i t = 5$, which is indicated by a vertical line. The instantaneous dispersion relations, shown in the bottom dual panels, imply that the real frequency and growth rate do not change much, but around $\Omega_i t = 5$, an abrupt change takes place. The instantaneous real frequency and growth rate at $\Omega_i t = 5$ are thus plotted. The wave energy density undergoes a somewhat sudden increase between $\Omega_i t = 5$ and $\Omega_i t = 10$, during which time the real frequency and growth rate continue to evolve. The snapshots of real frequency and growth rate at $\Omega_i t = 10$ are plotted in the bottom panels. Then between $\Omega_i t = 10$ and $\Omega_i t = 50$ the wave energy density undergoes a small increase, then somewhat steep reduction in intensity, followed by a gradual and monotonic decrease. The instantaneous dispersion relation at $\Omega_i t = 50$ and at the final time of $\Omega_i t = 100$ are plotted in the bottom panel. As one can see from the wave intensity profile, the excitation and saturation of EMIC instability are not clearly identifiable, as the early phase of EMIC instability development is intermingled with late phase of EFH instability evolution. This show the complex nature of the problem.

5 SUMMARY AND DISCUSSION

The solar wind is characterized by non-Maxwellian features associated with charged particles. Among such is the temperature anisotropy associated with ions (protons) and electrons. *In situ* measurements near 1 au reveal that the upper and lower bounds of the measured temperature ratios for these charged particles, $T_{\perp}/T_{\parallel i}$ and $T_{\perp}/T_{\parallel e}$, are bounded from above and below by various plasma instability threshold conditions. Consequently, many studies have been devoted to understanding various aspects of the temperature anisotropy-driven instabilities in the literature. Among these are electromagnetic ion cyclotron (or EMIC for short) and electron firehose (EFH) instabilities. It is customary to ignore the impacts of electrons in the study of EMIC instability, and also is the usual practice to assume isotropic protons in the study of EFH instability. However, as these two modes operate on the same branch of left-hand circularly polarized transverse electromagnetic dispersion relation, it is imperative that one treats both species equally. Moreover, it was shown (Yoon & Sarfraz 2017; Yoon et al. 2019) that the dynamically protons and electrons via excitations of these two modes play an important role in explaining the near isotropy of the solar wind plasma particles near 1 au. However, as the two unstable modes have distinct spatio-temporal scales, it is important to investigate their characteristics carefully. This could be an important issue if one wishes to generalize the scaled solar wind model considered by Yoon & Sarfraz (2017) and Yoon et al. (2019) to a realistic one.

This has prompted us to revisit the problem of dynamically coupled protons and electrons via excitation of combined EMIC and EFH instabilities, but in order to simplify the matter, we have restricted ourselves to uniform plasma. According to this paper, we found that for some parameter regime, EFH and EMIC operate on distinct time scales, which can be delineated clearly based upon the time profile of macroscopic quantities, that is, proton and electron betas as well as the wave magnetic field energy density. On the other hand, some other parameter regimes prevent such a clearcut distinction. In all the cases, however, the two instabilities operate on different spatio-temporal scales although they operate on the same left-hand circularly polarized dispersion curve. The findings from this paper may be useful in properly designing the realistic global model of the solar wind. This work can also be extended to include effects such as non-Maxwellian features, e.g. bi-kappa models (Lazar et al. 2017;

López et al. 2019), and in principle, to include obliquely propagating unstable modes (Paesold & Benz 1999; Li & Habbal 2000; López et al. 2019).

ACKNOWLEDGEMENTS

PHY acknowledges NASA Grant NNN18ZDA001N-HSR and NSF Grant 1842643 to the University of Maryland.

DATA AVAILABILITY

The data underlying this article will be shared on reasonable request to the corresponding author.

REFERENCES

Anderson B. J., Denton R. E., Ho G., Hamilton D. C., Fuselier S. A., Strangeway R. J., 1996, *J. Geophys. Res.*, 101, 21527

Baumjohann W., Treumann R. A., 2004, *Basic Space Plasma Physics*. Imperial College Press, London

Camporeale E., Burgess D., 2008, *J. Geophys. Res.*, 113, A07107

Chen L., Jordanova V. K., Spasojević M., Thorne R. M., Horne R. B., 2014, *J. Geophys. Res.*, 119, 2963

Chew G. F., Goldberger M. L., Low F. E., 1956, *Proc. R. Soc. A*, 236, 112

Davidson R. C., Ogden J. M., 1975, *Phys. Fluids*, 18, 1045

Dum C. T., Marsch E., Pilipp W., 1980, *J. Plasma Phys.*, 23, 91

Fried D. B., Conte S. D., 1961, *The Plasma Dispersion Function*. Academic Press, New York

Gary S. P., 1993, *Theory of Space Plasma Microinstabilities*. Cambridge Univ. Press, New York

Gary S. P., Nishimura K., 2003, *Phys. Plasmas*, 10, 3571

Gary S. P., McKean M. E., Winske D., Anderson B. J., Denton R. E., Fuselier S. A., 1994, *J. Geophys. Res.*, 99, 5903

Gary S. P., Vazquez V. M., Winske D., 1996, *J. Geophys. Res.*, 101, 13327

Gary S. P., Hughes R. S., Wang J., Chang O., 2014, *J. Geophys. Res.*, 119, 1429

Harris E. G., 1961, *J. Nucl. Energy, Part C, Plasma Phys.*, 2, 138

Hasegawa A., 1975, *Plasma Instabilities and Nonlinear Effects*. Springer-Verlag, New York

Hellinger P., Matsumoto H., 2000, *J. Geophys. Res.*, 105, 10519

Hellinger P., Trávníček P., Kasper J. C., Lazarus A. J., 2006, *Geophys. Res. Lett.*, 33, L09101

Hellinger P., Trávníček P. M., Decyk V. K., Schriver D., 2014, *J. Geophys. Res.*, 119, 59

Hollweg J. V., 1974, *J. Geophys. Res.*, 79, 3845

Hunana P., Zank G. P., 2017, *ApJ*, 839, 13

Isenberg P. A., Maruca B. A., Kasper J. C., 2013, *ApJ*, 773, 164

Lazar M., Poedts S., 2009a, *A&A*, 494, 311

Lazar M., Poedts S., 2009b, *Solar Phys.*, 258, 119

Lazar M., Poedts S., Schlickeiser R., Ibscher D., 2014, *Solar Phys.*, 289, 369

Lazar M., Poedts S., Schlickeiser R., Dumitraci C., 2015, *MNRAS*, 446, 3022

Lazar M., Shaaban S. M., Poedts S., Štverák Š., 2017, *MNRAS*, 464, 564

Lazar M., Yoon P. H., Lopez R. A., Moya P. S., 2018, *J. Geophys. Res. Space Phys.*, 123, 6

Li X., Habbal S. R., 2000, *J. Geophys. Res.*, 105, 27377

Lin R. P. et al., 1995, *Space Sci. Rev.*, 71, 125

López R. A., Lazar M., Shaaban S. M., Poedts S., Yoon P. H., Viñas A. F., Moya P. S., 2019, *ApJ*, 873, L20

Marsch E., Schwenn R., Rosenbauer H., Muehlhaeuser K.-H., Pilipp W., Neubauer F. M., 1982, *J. Geophys. Res.*, 87, 52

Marsch E., Ao X.-Z., Tu C.-Y., 2004, *J. Geophys. Res.*, 109, A04102

Marsch E., Zhao L., Tu C.-Y., 2006, *Ann. Geophys.*, 24, 2057

Maruca B. A., Kasper J. C., Gary S. P., 2012, *ApJ*, 748, 137

Maruca B. A., Kasper J. C., 2013, *Adv. Space Res.*, 52, 723

Matteini L., Landi S., Hellinger P., Velli M., 2006, *J. Geophys. Res.*, 111, A10101

Matteini L., Hellinger P., Landi S., Trávníček P. M., Velli M., 2012, *Space Sci. Rev.*, 172, 373

Messmer P., 2002, *A&A*, 382, 301

Ogilvie K. W. et al., 1995, *Space Sci. Rev.*, 71, 55

Omidi N., Isenberg P., Russell C. T., Jian L. K., Wei H. Y., 2014, *J. Geophys. Res.*, 119, 1442

Paesold G., Benz A. O., 1999, *A&A*, 351, 741

Phan T.-D., Paschmann G., Baumjohann W., Sckopke N., Lühr H., 1994, *J. Geophys. Res.*, 99, 121

Sagdeev R. Z., Shafranov V. D., 1961, *JETP*, 12, 130

Sarfraz M., Saeed S., Yoon P. H., Abbas G., Shah H. A., 2016, *J. Geophys. Res. Space Phys.*, 121, 9356

Sarfraz M., Yoon P. H., Saeed S., Abbas G., Shah H. A., 2017, *Phys. Plasmas*, 24, 012907

Schlickeiser R., 2002, *Cosmic Ray Astrophysics*. Springer-Verlag, Berlin

Schlickeiser R., Skoda T., 2010, *ApJ*, 716, 1596

Schlickeiser R., Lazar M., Skoda T., 2011, *Phys. Plasmas*, 18, 012103

Seough J. J., Yoon P. H., 2012, *J. Geophys. Res.*, 117, A08101

Seough J. J., Yoon P. H., Kim K.-H., Lee D. H., 2013, *Phys. Rev. Lett.*, 110, 071103

Seough J. J., Yoon P. H., Hwang J., 2014, *Phys. Plasmas*, 21, 062118

Seough J. J., Yoon P. H., Hwang J., 2015a, *Phys. Plasmas*, 22, 012303

Seough J. J., Yoon P. H., Hwang J., Nariyuki Y., 2015b, *Phys. Plasmas*, 22, 082122

Shaaban S. M., Lazar M., 2020, *MNRAS*, 492, 3529

Shaaban S. M., Lazar M., Poedts S., Elhanbaly A., 2015, *ApJ*, 814, 34

Shaaban S. M., Lazar M., Poedts S., Elhanbaly A., 2016, *J. Geophys. Res. Space Phys.*, 121, 6031

Shaaban S. M., Lazar M., Poedts S., Elhanbaly A., 2017, *Ap&SS*, 362, 13

Shaaban S. M., Lazar M., Yoon P. H., Poedts S., 2019a, *ApJ*, 871, 237

Shaaban S. M., Lazar M., Yoon P. H., Poedts S., 2019b, *A&A*, 627, A76

Štverák Š., Trávníček P., Maksimovic M., Marsch E., Fazakerley A. N., Scime E. E., 2008, *J. Geophys. Res.*, 113, A03103

Viñas A. F., Moya P. S., Navarro R., Araneda J. A., 2014, *Phys. Plasmas*, 21, 012902

Viñas A. F., Moya P. S., Navarro R. E., Valdivia J. A., Araneda J. A., Muñoz V., 2015, *J. Geophys. Res.*, 120, 3307

Wilson L. B. III, et al., 2018, *ApJS*, 236, 41

Wu C. S., Yoon P. H., Freund H. P., 1989, *Geophys. Res. Lett.*, 16, 1461

Yoon P. H., 1992, *Phys. Fluids B*, 4, 3627

Yoon P. H., 2017, *Rev. Mod. Plasma Phys.*, 1, 4

Yoon P. H., Sarfraz M., 2017, *ApJ*, 835, 246

Yoon P. H., Seough J. J., 2012, *J. Geophys. Res.*, 117, A08102

Yoon P. H., Seough J. J., 2014, *J. Geophys. Res.*, 119, 7108

Yoon P. H., Wu C. S., de Assis A. S., 1993, *Phys. Fluids B*, 5, 1971

Yoon P. H., Seough J. J., Kim K. H., Lee D. H., 2012, *J. Plasma Phys.*, 78, 47

Yoon P. H., Seough J. J., Hwang J., Nariyuki Y., 2015, *J. Geophys. Res.*, 120, 6071

Yoon P. H., López R. A., Seough J. J., Sarfraz M., 2017, *Phys. Plasmas*, 24, 112104

Yoon P. H., Seough J., Salem C. S., Klein K. G., 2019, *Phys. Rev. Lett.*, 123, 145101

Zhou Q., Xiao F., Shi J., Yang C., He Y., Tang L., 2013, *JGRA*, 118, 340